

# WGAST: Weakly-Supervised Generative Network for Daily 10 m Land Surface Temperature Estimation via Spatio-Temporal Fusion

Sofiane Bouaziz, Adel Hafiane, Raphaël Canals, Rachid Nedjai

**Abstract**—Urbanization, climate change, and agricultural stress are increasing the demand for precise and timely environmental monitoring. Land Surface Temperature (LST) is a key variable in this context and is retrieved from remote sensing satellites. However, these systems face a trade-off between spatial and temporal resolution. While spatio-temporal fusion methods offer promising solutions, few have addressed the estimation of daily LST at 10 m resolution. In this study, we present WGAST, a Weakly-Supervised Generative Network for Daily 10 m LST Estimation via Spatio-Temporal Fusion of Terra MODIS, Landsat 8, and Sentinel-2. WGAST is the first end-to-end deep learning framework designed for this task. It adopts a conditional generative adversarial architecture, with a generator composed of four stages: feature extraction, fusion, LST reconstruction, and noise suppression. The first stage employs a set of encoders to extract multi-level latent representations from the inputs, which are then fused in the second stage using cosine similarity, normalization, and temporal attention mechanisms. The third stage decodes the fused features into high-resolution LST, followed by a Gaussian filter to suppress high-frequency noise. Training follows a weakly supervised strategy based on physical averaging principles and reinforced by a PatchGAN discriminator. Experiments demonstrate that WGAST outperforms existing methods in both quantitative and qualitative evaluations. Compared to the best-performing baseline, on average, WGAST reduces RMSE by 17.18% and improves SSIM by 11.00%. Furthermore, WGAST is robust to cloud-induced LST and effectively captures fine-scale thermal patterns, as validated against 33 ground-based sensors. The code is available at <https://github.com/SofianeBouaziz1/WGAST.git>.

**Index Terms**—Spatio-temporal fusion, land surface temperature, spatial resolution, temporal resolution, generative adversarial networks.

## I. INTRODUCTION

CLIMATE change, rapid urbanization, and increasing environmental pressures are reshaping the dynamics of our planet with unprecedented speed [1]. Cities are expanding both in size and density, which makes issues like the Urban Heat Island (UHI) effect even worse [2]. At the same time, unpredictable weather patterns and changing ecosystems demand consistent attention and monitoring [3]. These phenomena are spatially and temporally complex, and tackling

This work was carried out as a part of the CHOISIR project funded by Orléans Métropole, and Région Centre-Val de Loire. (Corresponding author: Sofiane Bouaziz).

Sofiane Bouaziz and Adel Hafiane are with INSA Centre Val de Loire, Université d'Orléans, PRISME UR 4229, Bourges, 18022, Centre Val de Loire, France (e-mail: sofiane.bouaziz@insa-cvl.fr; adel.hafiane@insa-cvl.fr).

Sofiane Bouaziz and Raphaël Canals are with Université d'Orléans, INSA CVL, PRISME UR 4229, Orléans, 45067, Centre Val de Loire, France (e-mail: raphael.canals@univ-orleans.fr).

Rachid Nedjai is with Université d'Orléans, CEDETE, UR 1210, Orléans, 45067, Centre Val de Loire, France (e-mail: rachid.nedjai@univ-orleans.fr).

them requires reliable, fine-grained geospatial information with dense temporal frequency [4]. Detecting, monitoring, and predicting these challenges is essential to support sustainable urban planning [5], public health interventions [6], disaster response [7], and climate adaptation [8]. In this context, access to high-resolution environmental data is not only beneficial but crucial for making timely and informed decisions [9].

Land Surface Temperature (LST) is one of the most important geophysical variables for understanding and analyzing diverse environmental challenges. It is defined as the radiative skin temperature of the land surface, representing the complex interactions among incoming solar radiation, land cover, and atmospheric conditions [10]. LST is widely used across various domains, including climate change analysis [11], natural resource management [12], and urban planning [13]. It is regarded as a critical component of Earth system data by NASA [14], and is also identified as one of the ten essential climate variables by the Global Climate Observing System [15].

Remote sensing (RS) satellites remain the primary means for monitoring LST at regional to global scales [16]. These satellites retrieve LST through thermal infrared (TIR) sensors that measure the emitted radiation from the Earth's surface, which is then processed to estimate LST [17]. However, current RS satellites face a trade-off between spatial and temporal resolution. Spatial resolution refers to the level of surface detail captured within each pixel of an LST measurement [17], while temporal resolution indicates how frequently LST data are acquired for the same geographic area over time [18]. For instance, Terra MODIS provides daily LST data at a moderate 1 km resolution, whereas Landsat 8 offers finer 30 m resolution but revisits the same area every 16 days. Figure 1 illustrates this trade-off over the same geographic area. Figure 1.a shows how differences in spatial resolution affect the level of detail. For example, the Loire River, France's longest, is visible on Landsat 8 LST but not distinguishable on Terra MODIS LST. Figure 1.b highlights temporal resolution differences by showing that 16 daily Terra MODIS LST acquisitions occur between two Landsat 8 observations. Achieving high spatial and temporal resolution simultaneously remains challenging, but crucial to accurately capturing dynamic phenomena.

To overcome this trade-off, Spatio-Temporal Fusion (STF) techniques have emerged as a promising solution. These methods generate high spatial resolution satellite observations at finer temporal frequencies by combining data from different RS satellites with varying spatial and temporal characteristics [19]. Typically, one data source offers high spatial but low temporal resolution (HSLT), while the other provides

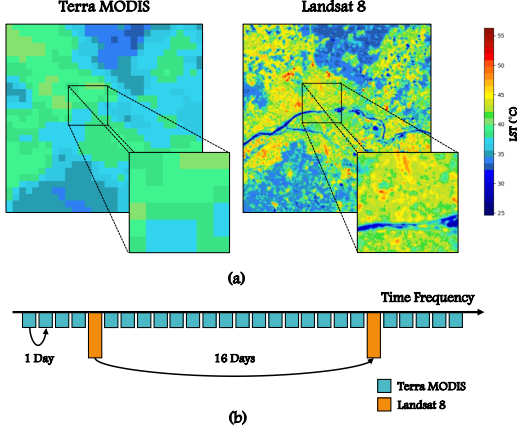


Fig. 1. LST resolution comparison over Orléans Métropole, France. (a) Spatial resolution difference between Terra MODIS and Landsat 8 on 13 Aug 2022. (b) Temporal resolution illustrated by their revisit frequencies.

low spatial but high temporal resolution (LSHT) [20]. STF methods were originally developed for producing fine spatio-temporal resolution surface reflectance (SR) imagery [19], [21], but empirical investigations have consistently demonstrated their strong performance when applied to LST estimation [9]. Existing STF approaches can be broadly classified into two main categories: traditional and learning-based methods. Traditional methods include three subtypes: weighted-based, unmixing-based, and hybrid methods. Among these, weighted-based methods are the most widely used. They predict fine spatio-temporal resolution images by leveraging data from spectrally similar neighboring pixels. A well-known example is STARFM [22], which incorporates moving windows and spatial similarity to estimate high-resolution observations. Its enhanced version, ESTARFM [23], improves the fusion by distinguishing between mixed and pure pixels. Although initially designed for SR data, these methods have also been adapted for LST. For instance, [24] applied STARFM to fuse Terra MODIS and ASTER data and generate ASTER-like LST products, while [25] employed ESTARFM to blend Terra MODIS and Landsat observations for producing LST at 100 m resolution. However, these traditional approaches rely on the key assumption that surface changes follow a linear trend over time. This assumption may hold for SR, but fails to accurately capture the non-linear and highly dynamic nature of LST [26]. Consequently, traditional methods often struggle to model the spatio-temporal variability of LST with sufficient accuracy.

Learning-based methods eliminate the linear assumption by leveraging data-driven models to capture complex spatio-temporal relationships directly from data. These models are trained using existing datasets to map the interactions between LSHT and HSLT LST. With deep learning (DL) advances, these models have become the most widely used approaches for STF. For example, [27] proposed STTFN, a residual multi-scale convolutional neural network to estimate fine-resolution LST. [28] utilized a conditional variational autoencoder framework to generate fine-resolution LST. More recently, [29] developed a two-stage hierarchical fusion model based on the Swin Transformer for enhanced LST estimation.

Among recent trends, generative adversarial networks (GANs) [30] have demonstrated notable success in image generation, including STF. In this setting, the generator learns to produce high-resolution fused images. At the same time, the discriminator is trained to distinguish between fused and real high-resolution samples, thus improving the realism and fidelity of the fusion output. Several GAN-based STF approaches have been proposed in the literature. For example, STFGAN [31] frames the STF task as a super-resolution problem. GAN-STFM [32] extends this approach by introducing conditional constraints, which enable a more flexible and context-aware fusion process. CycleGAN-STF [33] treats STF as a data augmentation task and selects the most informative image from cycle-consistent outputs as the final fusion result. MLFF-GAN [34] adopts a multilevel strategy by using a conditional GAN (cGAN), which models spatio-temporal dependencies across different levels. However, these methods have been primarily designed and validated using SR datasets. Applying them directly to LST is challenging due to the unique characteristics of thermal data [9]. As a result, adapting existing GAN-based STF methods to LST requires careful architectural adjustments and methodological considerations to ensure reliable performance.

All of the aforementioned STF methods generate fused LST observations at the minimum spatial resolution of the input satellites, which, at best, is 30 m. This resolution is provided by Landsat 8, the satellite offering the finest TIR band available in RS satellite products [35]. While this level of detail is sufficient for certain applications, it falls short in contexts where very high spatial precision is crucial. For example, studies focused on UHI require thermal observations at finer resolutions, such as 10 m, to capture intraurban temperature variations, and resolve narrow urban features like streets and small green spaces [36], [37]. Some recent studies have attempted to generate 10 m spatial resolution LST products while maintaining daily temporal frequency. For instance, [38] combines Terra MODIS and Sentinel-2 data using a robust least squares regression to produce daily 10 m LST. Similarly, [39] introduced mDTSG, which employs a convolution-based moving window to perform the STF between Terra MODIS and Sentinel-2. However, both approaches fall into the category of traditional STF methods and rely on the same linearity assumptions discussed earlier. These assumptions limit their ability to model the complex and spatiotemporal characteristics of LST. Also, the transition in spatial resolution from 1 km Terra MODIS to 10 m Sentinel-2 represents a 100× increase in detail which is extremely large. Performing fusion directly between these two sources without an intermediate resolution step introduces significant challenges as it amplifies noise and inconsistencies, and may generate unrealistic spatial patterns. Despite this, learning-based STF fusion methods, especially those utilizing DL, to generate daily 10 m LST observations remain largely unexplored. The only attempt, FuseTen [40], uses a hybrid model that combines a cGAN with linear regression by embedding a linear model within the generator, which can introduce artifacts and noise in the generated LST.

In this work, we address the identified research gap by introducing WGAST, a weakly-supervised generative network designed for daily 10 m LST estimation via STF. WGAST represents a novel deep generative framework and, to the best of our knowledge, is the first non-linear end-to-end DL model that simultaneously fuses Terra MODIS, Landsat 8, and Sentinel-2 observations to produce daily LST estimates at a 10 m resolution. Our key contributions are summarized as follows:

- We propose the first non-linear generative model specifically tailored for STF of LST, enabling accurate daily estimation at 10 m resolution by integrating coarse 1 km Terra MODIS data with complementary spectral information from Landsat 8 and Sentinel-2.
- We introduce Landsat 8 as an effective intermediate resolution bridge between Sentinel-2 and Terra MODIS, overcoming the extreme resolution gap and avoiding the direct, error-prone fusion from 1 km to 10 m.
- We design a novel, physically motivated weak supervision strategy that leverages 30 m Landsat-derived LST as proxy ground truth, to bypass the challenge of missing ground truth data at 10 m resolution.
- We eliminate the dependence on future observations for predicting the current time step by relying solely on a previous reference date.
- We generate 10 m LST with significantly fewer cloud-induced gaps than 30 m Landsat 8 by leveraging cloud-resilient Terra MODIS observations at the target time.
- We rigorously validate WGAST on two data sources, satellite and in-situ measurements, and both demonstrate its superiority in quantitative and qualitative evaluations compared to existing methods.

## II. PROBLEM FORMULATION

The STF problem for estimating daily 10 m LST can be formulated as follows. Let  $X_1$ ,  $X_2$ , and  $X_3$  denote RS satellites offering complementary spatial and temporal characteristics. We define  $r_s(\cdot)$  as the spatial resolution function where lower values indicate finer spatial detail, and  $r_t(\cdot)$  as the temporal resolution function where lower values indicate more frequent acquisitions. Let  $\text{TIR}(\cdot)$  be a predicate function returning `true` if the RS satellite provides TIR bands. The conditions defined in Equation 1 must be satisfied.

$$\begin{aligned} r_s(X_1) &> r_s(X_2) > r_s(X_3) \\ r_t(X_1) &< r_t(X_2) \\ r_s(X_3) &= 10 \text{ m}, \quad r_t(X_1) = 1 \text{ day} \\ \text{TIR}(X_1) &= \text{TIR}(X_2) = \text{true} \end{aligned} \quad (1)$$

In our setup,  $X_1$  corresponds to Terra MODIS, which provides daily LST at 1 km spatial resolution,  $X_2$  refers Landsat 8, which offers LST at 30 m with a 16-day revisit cycle, and  $X_3$  denotes Sentinel-2, which delivers SR data at 10 m with a 5-day revisit. These choices satisfy the conditions in Equation 1 and are summarized in Table I. Note that this formulation remains general and can be extended to any other RS missions as long as the conditions in Equation 1 are met.

TABLE I  
COMPARISON OF REPRESENTATIVE RS SATELLITES WITH THEIR  
THERMAL SENSORS, SPATIAL AND TEMPORAL RESOLUTIONS.

Satellite	Thermal sensor	Spatial resolution	Temporal resolution
Terra	MODIS	1 km	1 day
Landsat 8	TIRS	30 m	16 days
Sentinel-2	/	10 m	5 days

Given a target date  $t_2$ , the goal is to estimate LST at 10 m resolution, denoted as  $\hat{X}_3(s, t_2, \text{'LST'}, r_3)$ , where  $r_3 = 10 \text{ m}$ . To achieve this, we rely on the Terra MODIS LST observation  $X_1(s, t_2, \text{'LST'}, r_1)$  with  $r_1 = 1 \text{ km}$ , as well as a previous reference date  $t_1 < t_2$  chosen such that all three satellites  $X_1, X_2, X_3$  provide minimal cloud coverage observations over a geographic region  $s$ . At this reference date, we construct a prior triple  $T_1$  composed of the following observations:

- Sentinel-2 spectral indices at  $r_3 = 10 \text{ m}$ :  $X_3(s, t_1, \text{'NDVI'}, r_3)$ ,  $X_3(s, t_1, \text{'NDWI'}, r_3)$ , and  $X_3(s, t_1, \text{'NDBI'}, r_3)$ .
- Landsat 8 spectral indices at  $r_2 = 30 \text{ m}$ :  $X_2(s, t_1, \text{'NDVI'}, r_2)$ ,  $X_2(s, t_1, \text{'NDWI'}, r_2)$ , and  $X_2(s, t_1, \text{'NDBI'}, r_2)$ .
- Landsat 8 LST at  $r_2 = 30 \text{ m}$ :  $X_2(s, t_1, \text{'LST'}, r_2)$ .
- Terra MODIS LST at  $r_1 = 1 \text{ km}$ :  $X_1(s, t_1, \text{'LST'}, r_1)$ .

Where 'NDVI', 'NDWI', and 'NDBI' refer to spectral indices that characterize vegetation, water, and built-up surfaces, respectively. Their mathematical formulations are summarized in Table II. These indices are widely used in LST-related studies due to their strong correlation with land surface thermal behavior [41], [42]. While many other indices could be considered, we intentionally limit our selection to these three to ensure a diverse yet concise representation of surface types. This prevents introducing redundancy and avoids overloading the model with excessive input features, which could complicate training and hinder convergence.

TABLE II  
FORMULATIONS OF SPECTRAL INDICES FOR LANDSAT 8 AND  
SENTINEL-2. NIR: NEAR-INFRARED, SWIR: SHORTWAVE INFRARED,  
RED AND GREEN REFER TO VISIBLE BANDS.  $B_i$  DENOTES THE  $i$ -TH BAND  
OF THE CORRESPONDING SATELLITE SENSOR.

Index	Equation	Landsat 8	Sentinel-2
NDVI	$\text{NIR}-\text{Red}$	$B5-B4$	$B8-B4$
	$\text{NIR}+\text{Red}$	$B5+B4$	$B8+B4$
NDBI	$\text{SWIR}-\text{NIR}$	$B6-B5$	$B11-B8$
	$\text{SWIR}+\text{NIR}$	$B6+B5$	$B11+B8$
NDWI	$\text{Green}-\text{NIR}$	$B3-B5$	$B3-B8$
	$\text{Green}+\text{NIR}$	$B3+B5$	$B3+B8$

Thus, given the prior triple  $T_1$  and the Terra MODIS LST at  $t_2$ ,  $X_1(s, t_2, \text{'LST'}, r_1)$ , the STF task is formulated as the learning of a DL network  $f$ , parameterized by  $\mathbf{W}$ , to estimate the target LST at 10 m resolution, as defined in Equation 2.

$$\hat{X}_3(s, t_2, \text{'LST'}, r_3) = f(T_1, X_1(s, t_2, \text{'LST'}, r_1) | \mathbf{W}). \quad (2)$$

Here,  $T_1$  reflects the spatial and spectral context at the reference time  $t_1$ , while  $X_1(s, t_2, \text{'LST'}, r_1)$  provides the coarse resolution thermal information at the target time  $t_2$ . The

function  $f$  thus learns to integrate this information and project it into high-resolution thermal estimates  $\hat{X}_3(s, t_2, 'LST', r_3)$ . Note that WGAST relies solely on a previous date  $t_1$ , and thus eliminates the need to wait for a future overlapping period.

### III. METHODOLOGY

In this section, we first briefly review the basic structure of GANs and their conditional variant cGAN, as they form the foundation of our proposed approach. We then present the overall architecture WGAST. Finally, we describe in detail its main components: the generator, the weakly supervised learning strategy, and the discriminator.

#### A. Generative Adversarial Networks

GANs were first introduced by [30] and are widely regarded as a powerful class of deep generative models. They are based on a two-player adversarial game between two neural networks: a generator  $G$  and a discriminator  $D$  [43]. The generator aims to synthesize realistic data samples that mimic the distribution of real observations, while the discriminator attempts to distinguish between real data  $x \sim p_{\text{data}}$  and generated ones  $G(z)$ , where  $z \sim p_z$  is sampled from a latent prior distribution [44].

The discriminator outputs a probability map that indicates the likelihood that each input pixel is real or generated. It is optimized to maximize its classification accuracy, as expressed in Equation 3.

$$\mathcal{L}_D = \max_D \mathbb{E}_{x \sim p_{\text{data}}} [\log D(x)] + \mathbb{E}_{z \sim p_z} [\log(1 - D(G(z)))] \quad (3)$$

In contrast, the generator attempts to produce samples that fool the discriminator into classifying them as real. Its loss is defined in Equation 4.

$$\mathcal{L}^{(G)} = \min [ \log D(x) + \log(1 - D(G(z))) ] \quad (4)$$

The overall GAN training can be formulated as a minimax optimization problem as expressed in Equation 5.

$$L = \min_G \max_D [\log D(x) + \log(1 - D(G(z)))] \quad (5)$$

During training, the generator and discriminator engage in an adversarial interplay, as the generator improves its ability to produce convincing samples, the discriminator must also enhance its capacity to distinguish them from real ones. This iterative process drives both models to co-evolve and become increasingly competent. Theoretically, this dynamic converges to a Nash equilibrium [45], where the generator has learned the true data distribution so well that the discriminator can no longer reliably differentiate real from fake.

cGANs [46] extend the standard GAN framework by providing additional input information, known as the condition. This condition can take the form of class labels, images, or other contextual data, which guide the generator to produce outputs that are explicitly dependent on this information. As a result, cGANs enable more targeted, controllable, and context-aware generation, which is especially valuable for tasks where the output needs to be aligned with a specific input modality.

#### B. Overall Architecture

The overall architecture of WGAST is illustrated in Figure 2. Our framework is based on a cGAN, where the generation process is explicitly conditioned on the Terra MODIS LST observation at the target time. The objective is to estimate the LST at a fine spatial resolution of 10 m for a given geographical region  $s$  at a target time  $t_2$ . The generated output is denoted as  $\hat{X}_3(s, t_2, 'LST', r_3)$ , where  $r_3 = 10$  m.

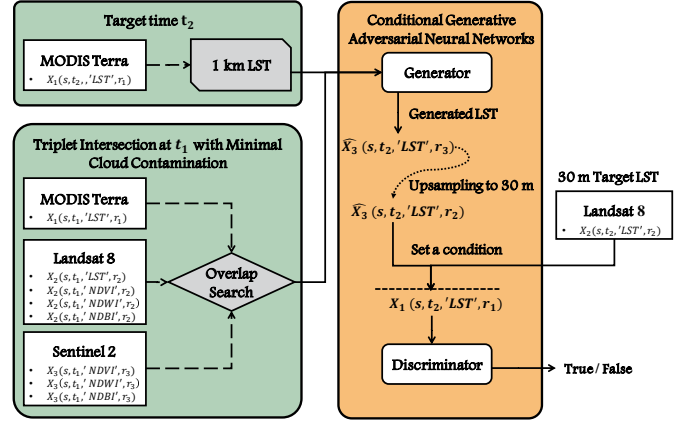


Fig. 2. Overview of the WGAST framework. WGAST consists of a generator that fuses data from Terra MODIS ( $r_1 = 1$  km), Landsat 8 ( $r_2 = 30$  m), and Sentinel-2 ( $r_3 = 10$  m) to produce a high-resolution LST estimate at 10 m. A discriminator ensures the quality of the generated LST by comparing it with the reference Landsat 8 LST at 30 m resolution.

The WGAST framework begins by identifying the overlapping timestep between the three RS satellites, as discussed in Section II, to extract the triple  $T_1$ . This triple, along with the Terra MODIS LST observation at the target time  $t_2$ ,  $X_1(s, t_2, 'LST', r_1)$  where  $r_1 = 1$  km, is used as input to the generator module. The generator is designed to capture relevant spatio-spectral and spatio-temporal features from the inputs to produce a fine-resolution LST observation at 10 m for the target date  $t_2$ . Since no ground-truth LST data at 10 m resolution are available, we adopt a weakly-supervised strategy motivated by physical principles. Specifically, the generated LST is averaged using a  $3 \times 3$  window to approximate a 30 m resolution. This output is then fed to the discriminator, which receives both the downsampled generated LST and a reference Landsat 8 30 m LST, each conditioned on the Terra MODIS LST observation at time  $t_2$ . Each component of the WGAST is detailed in the following subsections.

#### C. Generator

The generator module of WGAST consists of four main stages: *feature extraction*, *feature fusion*, *LST reconstruction*, and *noise suppression*.

1) *Feature extraction*: This stage employs a set of encoders composed of convolutional layers with downsampling and residual blocks, which are specifically designed to capture spatial and temporal features from the inputs. Batch Normalization layers are intentionally omitted from the residual blocks, as they degrade image synthesis quality in GANs [47].

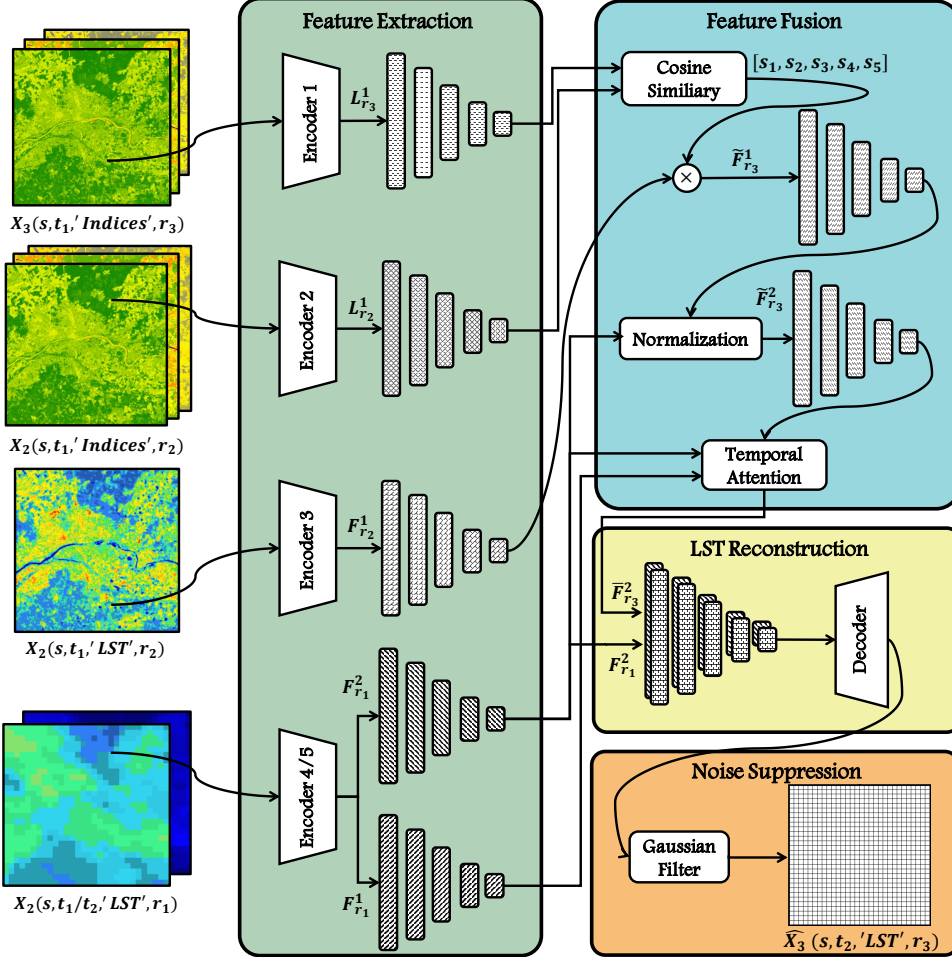


Fig. 3. Overall architecture of the WGAST Generator composed of four main stages: *feature extraction*, *feature fusion*, *LST reconstruction*, and *noise suppression*, with  $r_1 = 1 \text{ km}$ ,  $r_2 = 30 \text{ m}$ , and  $r_3 = 10 \text{ m}$ .

The extracted features are encoded into compact latent representations that enable the fusion stage to operate on the most informative abstractions. Specifically, five encoders are used, each producing a multi-level set of features as follows:

- *Encoder 1*: 10 m Sentinel-2 indices (NDVI, NDBI, NDWI) features at  $t_1$ , denoted as  $\mathbf{L}_{r_3}^1 = \{\mathbf{L}_{r_3,i}^1\}_{i=0}^N$ .
- *Encoder 2*: 30 m Landsat 8 indices (NDVI, NDBI, NDWI) features at  $t_1$ , denoted as  $\mathbf{L}_{r_2}^1 = \{\mathbf{L}_{r_2,i}^1\}_{i=0}^N$ .
- *Encoder 3*: 30 m Landsat 8 LST features at  $t_1$ , denoted as  $\mathbf{F}_{r_2}^1 = \{\mathbf{F}_{r_2,i}^1\}_{i=0}^N$ .
- *Encoder 4*: 1 km MODIS LST features at  $t_1$ , denoted as  $\mathbf{F}_{r_1}^1 = \{\mathbf{F}_{r_1,i}^1\}_{i=0}^N$ .
- *Encoder 5*: 1 km MODIS LST features at  $t_2$ , denoted as  $\mathbf{F}_{r_1}^2 = \{\mathbf{F}_{r_1,i}^2\}_{i=0}^N$ .

Here,  $N$  denotes the number of multi-level features produced by each encoder. Each feature group captures spatial or temporal characteristics at different levels of abstraction. Based on empirical evaluation, we fixed  $N = 5$  to ensure a good balance between feature richness and computational efficiency.

2) *Feature fusion*: The feature fusion process consists of three operations: *cosine similarity*, *normalization*, and *temporal attention*. The first operation, cosine similarity, is defined

#### Notations :

- $t_1, t_2$  : reference and target dates, respectively
- $X_1, X_2, X_3$  : Terra MODIS, Landsat 8, and Sentinel-2
- $L_{r_s}^1$  : spectral index features (NDVI, NDBI, NDWI) at spatial resolution  $r_s$  and date  $t_1$
- $F_{r_s}^1, F_{r_s}^2$  : LST features at spatial resolution  $r_s$  at  $t_1$  and  $t_2$  respectively
- $s_i$  : similarity score between feature pairs level  $i$
- $\tilde{F}_{r_3}^1, \tilde{F}_{r_3}^2, \tilde{F}_{r_3}^2$  : processed LST features at spatial resolution  $r_3$ :
  - $\tilde{F}_{r_3}^1$ : after cosine similarity (at  $t_1$ )
  - $\tilde{F}_{r_3}^2$ : after normalization (at  $t_2$ )
  - $\tilde{F}_{r_3}^2$ : after temporal attention (at  $t_2$ )

as follows. Given two feature vectors  $\mathbf{u}, \mathbf{v} \in \mathbb{R}^C$ , their cosine similarity is computed as expressed in Equation 6.

$$\text{cosine}_{\text{similarity}}(\mathbf{u}, \mathbf{v}) = \frac{\mathbf{u} \cdot \mathbf{v}}{\|\mathbf{u}\|_2 \cdot \|\mathbf{v}\|_2} \quad (6)$$

Where  $\|\cdot\|_2$  denotes the L2 norm. This metric measures the cosine of the angle between the two vectors, with values ranging from  $-1$  to  $1$ . A value of  $1$  indicates that the vectors are perfectly aligned in direction,  $0$  indicates no similarity, and  $-1$  indicates that the vectors are completely dissimilar in opposite directions. In the context of image feature maps, this operation is applied element-wise across the feature space.

The goal is to compute a similarity score between the multi-level features of Sentinel-2 indices at time  $t_1$ ,  $\mathbf{L}_{r_3}^1$ , and the multi-level features of Landsat 8 indices at the same time,  $\mathbf{L}_{r_2}^1$ . This score is then used to spatially refine the Landsat 8 LST features  $\mathbf{F}_{r_2}^1$ , to produce a 10 m features approximation of LST at time  $t_1$ , denoted as  $\tilde{\mathbf{F}}_{r_3}^1 = \{\tilde{\mathbf{F}}_{r_3,i}^1\}_{i=0}^N$ , where each level  $i$  is computed as in Equation 7.

$$\tilde{\mathbf{F}}_{r_3,i}^1 = \mathbf{F}_{r_2,i}^1 \odot \text{cos\_sim}(\mathbf{L}_{r_2,i}^1, \mathbf{L}_{r_3,i}^1) \quad (7)$$

Unlike linear models that assume a global linear relationship between indices and LST values, cosine similarity is a non-linear measure that captures local, level-wise structural correspondences between feature maps at different resolutions. This allows the refinement process to emphasize features that are both semantically meaningful and spatially aligned, leading to more accurate and context-aware estimations.

In the second operation, we employ *Adaptive Instance Normalization* (AdaIN) [48] to harmonize the statistical distributions between spatially detailed and temporally consistent features. Specifically, we align the structural content of the 10 m LST features extracted from the previous step,  $\tilde{\mathbf{F}}_{r_3}^1$ , with the style characteristics of the Terra MODIS LST features at time  $t_2$ ,  $\mathbf{F}_{r_1}^2$ . AdaIN proceeds in two steps. First, each level  $i$  of  $\tilde{\mathbf{F}}_{r_3}^1$  is normalized by removing its mean and standard deviation. Then, it is rescaled and shifted using the statistics of the style features  $\mathbf{F}_{r_1}^2$ . The operation is expressed in Equation 8.

$$\tilde{\mathbf{F}}_{r_3}^2 = \text{AdaIN}(\tilde{\mathbf{F}}_{r_3}^1, \mathbf{F}_{r_1}^2) = \sigma(\mathbf{F}_{r_1}^2) \cdot \frac{\tilde{\mathbf{F}}_{r_3}^1 - \mu(\tilde{\mathbf{F}}_{r_3}^1)}{\sigma(\tilde{\mathbf{F}}_{r_3}^1)} + \mu(\mathbf{F}_{r_1}^2) \quad (8)$$

Where  $\mu(\cdot)$  and  $\sigma(\cdot)$  denote the mean and standard deviation of feature map level  $i$ .

The final step, *temporal attention*, learns how temporal feature variations,  $\mathbf{F}_{r_1}^1$  and  $\mathbf{F}_{r_1}^2$ , influence the spatial feature structure. Its goal is to integrate this temporal information into the AdaIN-normalized spatial features  $\tilde{\mathbf{F}}_{r_3}^2$ . This is achieved through a spatially adaptive attention mechanism that estimates a set of attention weights  $\theta = \{\theta_i\}_{i=0}^N$ , where each  $\theta_i \in [0, 1]$  represents the relative importance of temporal features at level  $i$ . These weights are learned dynamically during training and control the influence of temporal variations in synthesizing the final 10 m feature representation at time  $t_2$ . Specifically, a  $1 \times 1$  convolution followed by batch normalization is applied to the Terra MODIS LST features at time  $t_1$  and  $t_2$ . This transformation projects the features into a more compact and discriminative space without altering their spatial resolution, making them more suitable for temporal comparison. It then computes the difference between these features to capture temporal variations. This difference is processed through another  $1 \times 1$  convolutional layer and a sigmoid activation to generate an attention mask. Finally, the mask is used to adaptively fuse the normalized spatial features with the temporal features at  $t_2$ . The full procedure is detailed in Algorithm 1.

3) *LST Reconstruction*: The reconstruction stage mirrors the encoder using a symmetric U-Net-like architecture with upsampling layers, transposed convolutions, and residual blocks to reconstruct the 10 m LST at time  $t_2$ . It takes as input the temporally-attended spatial features  $\tilde{\mathbf{F}}_{r_3}^2$  and the original MODIS LST features  $\mathbf{F}_{r_1}^2$ , concatenated along the channel dimension. Reintroducing  $\mathbf{F}_{r_1}^2$  at this stage helps preserve large-scale temperature patterns that may have been weakened during earlier fusion and normalization stages steps. The combined features are jointly decoded and progressively refined to produce the 10 m LST output, denoted as  $\hat{X}_3(s, t_2, \text{'LST'}, r_3)$ .

---

**Algorithm 1:** Temporal attention-based fusion

---

**Input:**  $\mathbf{F}_{r_1}^1$ : Terra MODIS LST features at time  $t_1$   
 $\mathbf{F}_{r_1}^2$ : Terra MODIS LST features at time  $t_2$   
 $\tilde{\mathbf{F}}_{r_3}^2$ : Normalized spatial features at time  $t_2$   
**Output:**  $\tilde{\mathbf{F}}_{r_3}^2$  : 10 m LST features at time  $t_2$

$$\tilde{\mathbf{F}}_{r_3}^2 \leftarrow [.] \cdot N$$

**foreach**  $i = 1, \dots, N$  **do**

/\* Apply a convolution with batch normalization to both Terra MODIS features at  $t_1$  and  $t_2$  \*/

$$F1 \leftarrow \text{Conv1x1\_BN}(\mathbf{F}_{r_1}^1[i])$$

$$F2 \leftarrow \text{Conv1x1\_BN}(\mathbf{F}_{r_1}^2[i])$$

/\* Compute the difference between the temporal features \*/

$$\Delta F \leftarrow F1 - F2$$

/\* Generate attention mask via convolution, BN, and sigmoid activation \*/

$$\theta_i \leftarrow \text{Sigmoid}(\text{Conv1x1\_BN}(\Delta F))$$

/\* Compute the weighted sum of spatial features \*/

$$\tilde{\mathbf{F}}_{r_3}^2[i] \leftarrow F_{r_1}^2[i] \cdot \theta_i + \tilde{\mathbf{F}}_{r_3}^2[i] \cdot (1 - \theta_i)$$

**return**  $\tilde{\mathbf{F}}_{r_3}^2$

---

4) *Noise Suppression*: The *noise suppression* module reduces high-frequency artifacts present in the reconstructed LST output  $\hat{X}_3(s, t_2, \text{'LST'}, r_3)$ , to produce a more spatially and temporally coherent result, denoted as  $\hat{X}_3(s, t_2, \text{'LST'}, r_3)$ . This step is essential, as LST in geophysical contexts exhibits smooth, spatially continuous patterns resulting from heat diffusion, rather than abrupt variations or isolated spikes. However, generators, especially those with multiple upsampling layers and skip connections, can unintentionally amplify pixel-level noise and produce unrealistic high-frequency textures that deviate from the expected physical smoothness of LST. To address this, we apply a classical Gaussian filter, which smooths the image by convolving it with a Gaussian kernel, thereby attenuating local fluctuations while preserving the essential spatial structure and coherence of LST. The Gaussian kernel is defined in Equation 9.

$$G(x, y; \sigma) = \frac{1}{2\pi\sigma^2} \exp\left(-\frac{x^2 + y^2}{2\sigma^2}\right), \quad (9)$$

where  $\sigma$  is the standard deviation that controls the degree of smoothing. The higher the value of  $\sigma$ , the stronger the smoothing effect. This kernel is centered at the origin and has a mean of zero. In WGAST,  $\sigma$  is fixed to 1.

The noise suppression is then carried out by applying a Gaussian smoothing filter to the predicted LST through a depthwise convolution with a fixed kernel as defined in Equation 10.

$$\hat{X}_3(s, t_2, \text{'LST'}, r_3) = \text{Conv2D}(\tilde{X}_3(s, t_2, \text{'LST'}, r_3), G(x, y; \tau)), \quad (10)$$

Where  $G(x, y; \tau)$  is the two-dimensional Gaussian kernel defined in Equation 9. The kernel size is computed as  $k = 2 \cdot \lceil 3\sigma \rceil + 1$ . Reflective padding is employed to mitigate boundary artifacts.

#### D. Weakly Supervised Learning

In the absence of ground-truth LST data at 10 m resolution, we adopt a weakly supervised learning strategy guided by physical principles. Prior studies have demonstrated that LST at coarser spatial resolutions can often be approximated by local averages of finer resolution values [49]. Specifically, under the assumption of limited thermal variability within small areas, a 30 m LST value can be approximated by averaging a  $3 \times 3$  neighborhood of 10 m pixels.

Leveraging this insight, we apply a  $3 \times 3$  average pooling operation to the generator's output  $\hat{X}_3(s, t_2, 'LST', r_2)$  to produce a 30 m estimate, as shown in Equation 11. This upsampled output is then compared to the corresponding Landsat 8 LST observation at time  $t_2$ ,  $X_2(s, t_2, 'LST', r_2)$ . The Landsat 8 LST is used solely during training. This enables the model to rely exclusively on the temporally frequent Terra MODIS inputs at inference time, thus preserving the 1-day revisit temporal resolution.

$$\hat{X}_3(s, t_2, 'LST', r_2)(m, n) = \frac{1}{9} \sum_{i=0}^2 \sum_{j=0}^2 \hat{X}_3(s, t_2, 'LST', r_3)(3m + i, 3n + j) \quad (11)$$

#### E. Discriminator

WGAST discriminator is based on the PatchGAN architecture [30]. Unlike traditional GANs that distinguish real from fake images, here the discriminator's task is to differentiate between observed LST data and fused LST outputs. The discriminator receives as input the LST image conditioned on the corresponding Terra MODIS observation  $X_1(s, t_2, 'LST', r_1)$ , which provides reliable thermal context at 1 km resolution. This conditioning enhances the discriminator's ability to assess whether the target LST image aligns with physically plausible thermal patterns reflected by the MODIS data. The final layer applies a softmax function to output probabilities. During training, the discriminator should output a probability close to 1 when fed with the observed Landsat 8 LST  $X_2(s, t_2, 'LST', r_2)$  alongside the Terra MODIS input, indicating real LST data. Conversely, it is expected to output a probability close to 0 when presented with the fused LST output  $\hat{X}_3(s, t_2, 'LST', r_2)$  paired with the Terra MODIS LST.

#### F. Loss Functions

1) *Discriminator Loss*: The discriminator is trained to distinguish between real LST observations and the generated fused LST outputs. The discriminator loss, denoted as  $\mathcal{L}_D$ , is defined in Equation 12. For brevity, we use the notation  $\hat{X}_3('LST', r_2)$  to represent  $\hat{X}_3(s, t_2, 'LST', r_2)$ , and similarly for  $X_2$  and  $X_1$ .

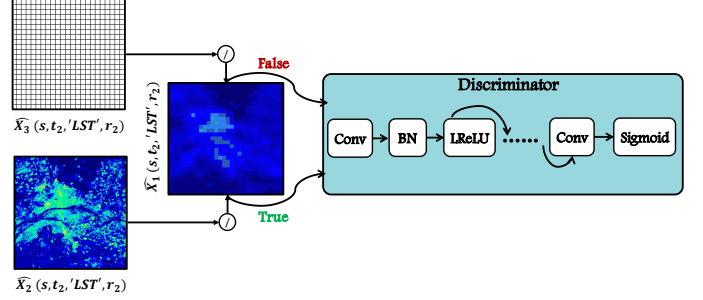


Fig. 4. WGAST discriminator based on the PatchGAN architecture.

$$\begin{aligned} \mathcal{L}_D = & \frac{1}{2} \mathbb{E}_{\hat{X}_3, X_1} \left[ \left( D \left( \hat{X}_3('LST', r_2) \mid X_1('LST', r_2) \right) \right)^2 \right] \\ & + \frac{1}{2} \mathbb{E}_{X_2, X_1} \left[ \left( D \left( X_2('LST', r_2) \mid X_1('LST', r_2) \right) - 1 \right)^2 \right] \end{aligned} \quad (12)$$

Where  $D(\cdot)$  denotes the discriminator. The loss adopts the least-squares GAN formulation [50], which penalizes the discriminator for assigning values far from 0 for fake generated LST and far from 1 for real LST, thereby stabilizing training and mitigating vanishing gradients. The expectations  $\mathbb{E}$ . denote averages taken over training samples.

2) *Generator Loss*: The generator loss, denoted by  $\mathcal{L}_G$ , combines adversarial feedback with several image-based losses to ensure both realism and fidelity in the fused output. The full loss formulation is given in Equation 13.

$$\begin{aligned} \mathcal{L}_G = & \underbrace{\alpha \mathbb{E}_{\hat{X}_3, X_1} \left[ \left( D \left( \hat{X}_3('LST', r_2) \mid X_1('LST', r_2) \right) - 1 \right)^2 \right]}_{\mathcal{L}_{GAN}} \\ & + \beta \underbrace{\frac{1}{K} \sum_{k=1}^K \left| \hat{X}_3('LST', r_2) - X_2('LST', r_2) \right|}_{\mathcal{L}_{content}} \\ & + \gamma \underbrace{1 - \frac{\langle \hat{X}_3('LST', r_2), X_2('LST', r_2) \rangle}{\| \hat{X}_3('LST', r_2) \|_2 \| X_2('LST', r_2) \|_2}}_{\mathcal{L}_{spectrum}} \\ & + \delta \underbrace{1 - \text{MS-SSIM} \left( \hat{X}_3('LST', r_2), X_2('LST', r_2) \right)}_{\mathcal{L}_{vision}} \end{aligned} \quad (13)$$

Where, the adversarial loss  $\mathcal{L}_{GAN}$  encourages the generator to produce fused LST outputs  $\hat{X}_3(s, t_2, 'LST', r_2)$  that the discriminator cannot distinguish from real high-resolution LST observations, conditioned on the corresponding low-resolution image  $X_1(s, t_2, 'LST', r_1)$ . The content loss  $\mathcal{L}_{content}$  is computed as the pixel-wise L1 distance between the generated and real high-resolution LST outputs, which promotes numerical accuracy. The spectrum loss  $\mathcal{L}_{spectrum}$ , defined as one minus the cosine similarity, preserves the overall spatial variation and temperature distribution. Lastly, the vision loss  $\mathcal{L}_{vision}$  is derived from the Multiscale Structural Similarity Index (MS-SSIM) and captures perceptual and structural coherence across multiple spatial scales.

## IV. EXPERIMENTAL RESULTS

### A. Region of Interest

The region of interest (ROI) is located within Orléans Métropole, France. As illustrated in Fig. 5(a1), the ROI is geographically situated between latitudes  $47^{\circ}50'41.77''\text{N}$  and  $47^{\circ}54'1.74''\text{N}$ , and longitudes  $1^{\circ}50'6.98''\text{E}$  and  $1^{\circ}59'36.36''\text{E}$ , covering an area of approximately  $114\text{ km}^2$ . It is traversed by the Loire River, France's longest river, which plays a prominent geographical and thermal role in the region (Fig. 5(a2)). This ROI presents a rich mosaic of land cover types, including dense urban areas, open water bodies, natural forests, industrial zones, and crop fields (Fig. 5(b1)–(b5)). Such heterogeneity introduces a wide range of radiative, thermal, and textural surface characteristics, which pose challenges for accurate LST prediction. Consequently, this makes it a suitable benchmark for evaluating the spatial adaptability and generalization capacity of WGAST, particularly in heterogeneous urban settings where LST can vary sharply over short distances.

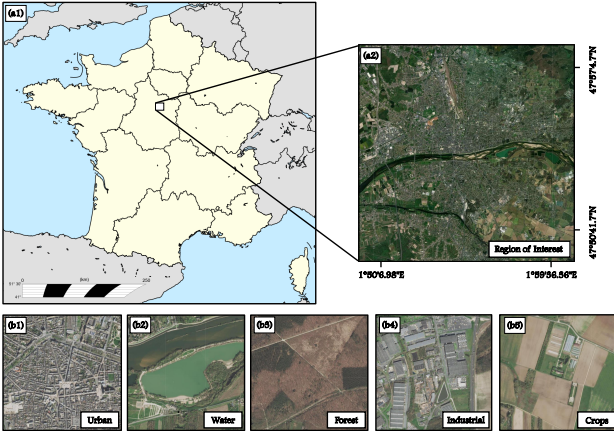


Fig. 5. Geographic overview of the ROI. (a1) Position of the ROI within France. (a2) High-resolution satellite image of the ROI. (b1)–(b5) Representative examples of key land cover categories observed in the ROI: urban, water, forest, industrial, and agricultural zones.

### B. Datasets

1) *Satellite Data*: The RS satellite data  $X_1$ ,  $X_2$ , and  $X_3$  were obtained from the Google Earth Engine (GEE) platform [51]. Terra MODIS data were accessed from the MOD11A1 (Collection 6.1) daily 1 km product on GEE, which provides atmospherically corrected LST values through the *LST\_Day\_1km* band, with a reported RMSE within  $2^{\circ}\text{C}$  for most land cover types [52]. Landsat 8 data were retrieved from the USGS Level-2 Collection 2 Tier 1 dataset on GEE. The thermal band *ST\_B10* was used to obtain LST, which is estimated using a single-channel algorithm based on Band 10, with an accuracy of approximately  $1.5^{\circ}\text{C}$  [53]. NDVI, NDWI, and NDBI were computed from the SR bands *SR\_B3*, *SR\_B4*, *SR\_B5*, and *SR\_B6*. Sentinel-2 imagery was collected from the Harmonized MSI Level-2A collection, which is also atmospherically corrected. NDVI, NDWI, and NDBI were calculated using SR bands *B2*, *B3*, *B4*, *B8*, and *B11*. Table III presents the 11 selected samples, each consisting of a previous

reference date  $t_1$  and a target date  $t_2$ . At  $t_1$ , we ensured spatial and temporal overlap among Terra MODIS, Landsat 8, and Sentinel-2 acquisitions. At  $t_2$ , WGAST uses only Terra MODIS LST data as input, while Landsat 8 LST is reserved for evaluation purposes. As an illustrative example, consider the prediction task for 23 Feb 2018. To estimate the 10 m LST at this date ( $t_2$ ), WGAST takes as input the Terra MODIS LST at  $t_2$ , along with the triple  $T_1$  extracted from the previous reference date 09 April 2017 ( $t_1$ ). The model then generates a fused LST at 10 m resolution, which is then upsampled and compared against the Landsat 8 LST acquired on 23 Feb 2018.

Notably, the acquisition times of the RS satellites are closely aligned, with a maximum time difference of approximately 1 hour and 15 minutes. These overpasses occur within the mid-morning window between 10:00 and 12:00 local time, a period typically characterized by stable surface and atmospheric conditions. As a result, variations in both LST and SR are minimal. This tight temporal alignment further reinforces the suitability of the fusion process. Each observation has a resolution of  $1200 \times 1200$  pixels for Sentinel-2, which corresponds to  $400 \times 400$  pixels for Landsat-8. All selected samples exhibit cloud contamination levels below 20%. Missing values caused by cloud cover or technical issues were filled using an adaptive spatial interpolation. Specifically, for each missing pixel, a local mean filter was applied within a  $3 \times 3$  window centered on the pixel. If no valid neighbors were found, the window size was progressively expanded in steps of 2 until at least one valid neighboring pixel was included.

The first 7 samples were used for training, with a patch size of  $96 \times 96$  and a stride of 24 for Sentinel-2 (respectively,  $32 \times 32$  and a stride of 8 for Landsat 8), resulting in a total of 15,463 training patches. The remaining 4 samples were reserved for testing. To avoid temporal data leakage and ensure that the model learns meaningful generalization patterns, no overlap was allowed between the reference and target dates across different training samples. Specifically, the reference date  $t_1$  of a sample  $i$  was not permitted to match the target date  $t_2$  of sample  $i-1$ , and vice versa. For testing, such constraints were not necessary since each test sample is treated as fully independent from the others. WGAST was trained with a learning rate of  $2 \times 10^{-4}$  and a batch size of 32 on a physical server equipped with an NVIDIA RTX A6000 GPU.

2) *In-situ Measurement*: To validate WGAST under real-world conditions, we leveraged a network of 33 ground-based sensors distributed across the ROI, each recording ambient air temperature ( $T_a$ ) at a height of 2.10 meters following standard meteorological protocols. The validation period spanned from 1 April 2025 to 30 May 2025, during which 25 cloud-free Terra MODIS LST images were acquired. Accordingly, WGAST was applied to generate 25 10 m LST observations corresponding to these dates. Figure 6 illustrates the spatial distribution of the sensors. It is worth emphasizing that, during the same period, only two Landsat 8 LST acquisitions were available, on 01 May 2025 and 17 May 2025, both of which were partially affected by cloud contamination. Moreover, no usable Landsat 8 data were available for April due to persistent cloud cover and technical issues. In stark contrast, our ap-

TABLE III

SUMMARY OF THE 11 SELECTED SAMPLES, EACH CONSISTING OF A REFERENCE TIME STEP ( $t_1$ ) AND A CORRESPONDING TARGET TIME STEP ( $t_2$ ) USED FOR PREDICTION.

Sample No.	Reference Date $t_1$				Target Date $t_2$		
	Date	Terra MODIS	Landsat 8	Sentinel-2	Date	Terra MODIS	Landsat 8
1	09 Apr 2017	11:54	10:40	11:05	23 Feb 2018	11:54	10:40
2	21 Oct 2018	11:54	10:41	11:06	26 Feb 2019	11:54	10:40
3	06 Sep 2019	11:54	10:41	11:07	01 Apr 2020	11:54	10:40
4	22 Jul 2020	11:54	10:41	11:07	07 Aug 2020	11:54	10:41
5	06 Mar 2022	11:48	10:41	10:57	22 Mar 2022	11:48	10:41
6	13 Aug 2022	11:42	10:41	10:57	29 Aug 2022	11:42	10:41
7	28 May 2023	11:10	10:40	11:07	13 Jun 2023	10:36	10:40
8	12 Apr 2024	10:35	10:40	11:07	19 Sep 2024	10:00	10:41
9	19 Sep 2024	10:00	10:41	11:07	05 Oct 2024	10:48	10:41
10	19 Sep 2024	10:00	10:41	11:07	21 Oct 2024	10:06	10:41
11	19 Sep 2024	10:00	10:41	11:07	01 May 2025	09:30	10:40

proach successfully generated 25 cloud-free LST observations at 10 m resolution over the same timeframe.

Although  $T_a$  and LST are fundamentally distinct physical quantities, they are known to exhibit strong radiative coupling, particularly under clear-sky and daytime conditions. This coupling makes air temperature a reliable proxy for indirectly assessing the consistency and physical realism of WGAST's fused LST outputs.

Field observations revealed that  $T_a$  measured by the ground sensors remains relatively stable within a 10 m spatial window. This stability makes it highly comparable to the 10 m resolution LST maps generated by WGAST. Thus, we extracted the exact geographic coordinates of each sensor location from the fused LST maps and assigned the corresponding 10 m  $\times$  10 m pixel value as the representative LST. This resulted in a spatially aligned dataset of paired  $T_a$  and LST values.



Fig. 6. Spatial distribution of sensors across the ROI. The central map displays the overall sensor locations marked with orange dots. At the same time, the zoomed-in insets highlight the detailed placement of selected sensors (Sensor 03, Sensor 06, Sensor 13, Sensor 17, Sensor 21, and Sensor 31) within their immediate surroundings.

### C. Quantitative Assessment

1) *Convergence Analysis*: Figure 7 presents the training evolution of both the generator and discriminator losses throughout the adversarial training process. Initially, the generator loss is relatively high, starting at approximately 2.53,

which is expected since the generator has not yet learned the complex spatio-spectral and spatio-temporal relationships within the input data. As training progresses and the generator improves its ability to produce more realistic fused LST images, this loss steadily decreases, reaching around 0.58 by the end of training. In contrast, the discriminator starts with a very low loss of about 0.07, which indicates that distinguishing between real and generated LST data is relatively easy at the beginning of training, since the fused LST images are still of low quality. However, as the generator improves and the quality of fused LST images increases, the discriminator's task becomes more challenging, resulting in a gradual increase in its loss. This opposing behavior reflects the adversarial nature of cGANs. Ultimately, both the generator and discriminator losses tend to stabilize and approach the Nash equilibrium, which indicates that the training process is converging.

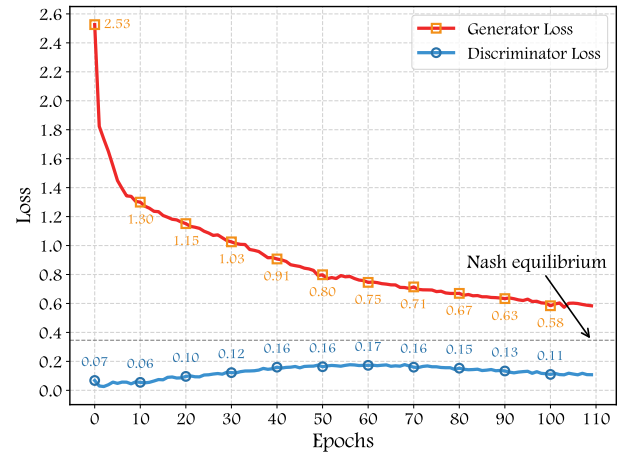


Fig. 7. Evolution of generator and discriminator losses during WGAT's training. The generator loss decreases steadily as it learns to produce more realistic fused LST, while the discriminator loss increases as its task becomes more challenging. Both losses eventually stabilize.

2) *Model Performance Analysis*: The evaluation of WGAST was conducted over four distinct dates using six well-established metrics. Two of these are error assessment metrics: Root Mean Square Error (RMSE) and Error Relative

TABLE IV  
QUANTITATIVE COMPARISON OF WGAST AGAINST BICUBIC1, TEN-ST-GEE [38], AND FUSETEN [40] OVER FOUR DATES.

Metric	Bicubic1	Ten-ST-GEE	FuseTen	WGAST	Bicubic1	Ten-ST-GEE	FuseTen	WGAST
<b>19 Sep 2024</b>					<b>05 Oct 2024</b>			
RMSE (↓)	3.637	3.934	3.220	<b>2.609</b>	2.451	2.583	<b>1.050</b>	1.384
SSIM (↑)	0.640	0.526	0.798	<b>0.813</b>	0.666	0.621	0.863	<b>0.910</b>
PSNR (↑)	15.357	14.503	18.552	<b>21.416</b>	17.765	17.310	<b>25.657</b>	24.992
SAM (↓)	4.841	6.168	<b>3.865</b>	5.410	3.162	6.158	<b>2.823</b>	3.579
CC (↑)	0.572	-0.025	<b>0.814</b>	0.748	0.571	0.113	<b>0.901</b>	0.861
ERGAS (↓)	4.595	4.983	3.944	<b>3.297</b>	4.190	4.447	<b>1.795</b>	2.365
<b>21 Oct 2024</b>					<b>01 May 2025</b>			
RMSE (↓)	2.150	2.342	1.905	<b>1.482</b>	4.724	5.340	3.234	<b>2.318</b>
SSIM (↑)	0.770	0.837	0.867	<b>0.893</b>	0.538	0.707	0.790	<b>0.838</b>
PSNR (↑)	18.450	24.592	21.748	<b>25.338</b>	16.186	21.281	19.476	<b>23.080</b>
SAM (↓)	3.930	4.689	<b>3.033</b>	3.650	5.823	7.625	3.918	<b>3.885</b>
CC (↑)	0.494	0.120	<b>0.896</b>	0.887	0.538	0.095	<b>0.840</b>	0.826
ERGAS (↓)	3.315	3.610	2.937	<b>2.285</b>	4.819	5.515	3.300	<b>2.364</b>

Global Dimensionless Synthesis (ERGAS), which quantify the pixel-wise discrepancies between the generated and reference LST. The remaining four are quality assessment metrics: Structural Similarity Index Measure (SSIM), Peak Signal-to-Noise Ratio (PSNR), Spectral Angle Mapper (SAM), and Correlation Coefficient (CC), all of which evaluate the perceptual, spectral, and structural fidelity of the results. For performance evaluation, the predicted 10 m LSTs were averaged within a  $3 \times 3$  window to match the 30 m resolution, and then validated against the Landsat 8 LST. We compare our approach against three existing methods. The first is Bicubic1, which performs a straightforward bicubic interpolation to upscale Terra MODIS LST data to Sentinel-2 resolution, in order to produce daily LST at 10 m. The second is Ten-ST-GEE [38], which assumes a linear relationship for the fusion task and employs robust least squares fusion of Terra MODIS and Sentinel-2 data within the GEE framework to generate daily LST at 10 m resolution. The third is FuseTen [40], which employs a hybrid model combining a cGAN with linear regression. Table IV presents the quantitative results obtained across the four evaluation dates and the six performance metrics. Note that the task of generating daily 10 m LST using a full DL model has not been previously addressed in the literature. FuseTen represents the only existing attempt at this spatial resolution by employing a hybrid linear-DL model. Most existing methods focus on producing daily LST at 30 m resolution, and thus were not included in our comparison, as they are not directly applicable to the finer 10 m spatial scale targeted by WGAST.

On 19 Sep 2024, WGAST outperforms all competing methods across most metrics, with the exception of SAM and CC. Compared to FuseTen, WGAST reduces the RMSE by 18.98%, indicating more accurate pixel-wise LST estimates. It also achieves a 1.88% increase in SSIM, which reflects better preservation of spatial structure and textures. In terms of radiometric quality, PSNR improves by 15.44%, and ERGAS decreases by 16.40%, highlighting enhanced global spectral fidelity. Although WGAST shows a slightly higher SAM and a marginally lower CC than FuseTen, these results can be

attributed to its focus on preserving local spatial details and structural sharpness, occasionally at the expense of global angular alignment and correlation. When compared to Ten-ST-GEE, the improvements are even more pronounced. WGAST achieves a 33.68% reduction in RMSE, a 54.56% increase in SSIM, a 47.67% gain in PSNR, and a 33.84% decrease in ERGAS. On 05 Oct 2024, WGAST demonstrates performance comparable to that of FuseTen, though it does not surpass it across all metrics. For example, WGAST achieves an RMSE of 1.384, which is only 0.334 higher than the 1.050 obtained by FuseTen. Similar patterns are observed in PSNR, SAM, CC, and ERGAS. Nevertheless, WGAST improves the SSIM by 5.45% compared to FuseTen. On 21 Oct 2024, WGAST delivers strong performance across all evaluation metrics. Compared to FuseTen, it achieves a 22.20% reduction in RMSE, a 3.00% increase in SSIM, a 16.50% gain in PSNR, and a 22.20% decrease in ERGAS. In comparison to Ten-ST-GEE, WGAST achieves a 36.73% reduction in RMSE, a 6.69% improvement in SSIM, a 3.03% increase in PSNR, and a 36.70% reduction in ERGAS. On 01 May 2025, despite the large temporal gap from the reference date at  $t_1$  (19 Sep 2024), WGAST maintains strong performance, while other methods show notable accuracy degradation. For instance, compared to FuseTen, WGAST achieves a 28.32% improvement in RMSE, a 6.08% gain in SSIM, a 18.50% increase in PSNR, a 0.84% decrease in SAM, and a 28.36% reduction in ERGAS.

On average across all test dates, as described in Table V, compared to FuseTen, WGAST reduces RMSE by 17.18%, improves SSIM by 4.10%, increases PSNR by 11.00%, and decreases ERGAS by 13.90%. When compared to the best linear method, the improvements are even more substantial, with a 39.90% reduction in RMSE, a 28.38% increase in SSIM, a 22.06% gain in PSNR, and a 36.70% decrease in ERGAS. This demonstrates consistent superiority across evaluation metrics.

3) *In-situ Measurement*: LST and air temperature ( $T_a$ ) are fundamentally distinct physical quantities. However, under clear-sky and daytime conditions, they exhibit strong radiative

TABLE V  
AVERAGE QUANTITATIVE COMPARISON OF ALL METHODS.

Metric	Bicubic1	Ten-ST-GEE	FuseTen	WGAST
	Average			
RMSE (↓)	3.241	3.550	2.352	<b>1.948</b>
SSIM (↑)	0.654	0.673	0.830	<b>0.864</b>
PSNR (↑)	16.940	19.422	21.358	<b>23.707</b>
SAM (↓)	4.439	6.160	<b>3.410</b>	4.131
CC (↑)	0.544	0.076	<b>0.863</b>	0.831
ERGAS (↓)	4.073	4.645	2.994	<b>2.578</b>

coupling due to energy exchanges between the land surface and the atmosphere. This often leads to coherent spatial and temporal patterns, even though their absolute values may differ. Accordingly, a high correlation between the fused 10 m LST and ground-based  $T_a$  is a meaningful indicator of the physical realism and internal consistency of the predicted LST. To quantify this relationship, we employed two correlation metrics: the Pearson correlation coefficient (PCC) and the Spearman rank correlation coefficient (SRCC). PCC quantifies the strength and direction of a linear relationship between two continuous variables [54]. Its value ranges from  $-1$  to  $1$ , where  $1$  denotes a perfect positive linear correlation,  $-1$  denotes a perfect negative linear correlation, and  $0$  indicates no linear dependence. Given two variables  $a$  and  $b$ , PCC is defined as shown in Equation 14, where  $\text{cov}(a, b)$  denotes the covariance between  $a$  and  $b$ , and  $\sigma_a$ ,  $\sigma_b$  are their standard deviations.

$$\text{PCC} = \frac{\text{cov}(a, b)}{\sigma_a \sigma_b} \quad (14)$$

SRCC measures the strength and direction of a monotonic relationship between two variables [55]. Unlike PCC, it operates on rank-transformed values rather than raw measurements, where each value is replaced by its position in the sorted list. This makes SRCC well-suited for ordinal or non-linear monotonic relationships. Given two variables  $u$  and  $v$ , with ranks  $R(u)$  and  $R(v)$ , SRCC  $\rho$  is defined in Equation 15.

$$\text{SRCC} = 1 - \frac{6 \sum_{i=1}^m d_i^2}{m(m^2 - 1)} \quad (15)$$

where  $d_i = R(a_i) - R(b_i)$  is the difference between the ranks of the  $i$ -th values of the two variables, and  $m$  is the total number of paired data. SRCC ranges from  $-1$  to  $1$ , with values near either extreme indicating strong monotonic relationships.

Table VI presents the PCC and SRCC results between the WGAST's 10 m pixel-wise generated LST and the corresponding ground-based air temperature ( $T_a$ ) measurements across 33 sensors. The results reveal consistently strong correlations, with PCC values ranging from 0.80 to 0.95 and SRCC values from 0.80 to 0.94. These high correlations indicate a strong and statistically meaningful relationship between generated LST and ( $T_a$ ), which supports the physical realism and consistency of WGAST's fused 10 m LST. Notably, even the lowest values exceed commonly accepted thresholds, which highlights the method's robustness across diverse sensor locations and urban conditions. Overall, this performance underscores

TABLE VI  
PCC AND SRCC BETWEEN FUSED LST AND GROUND AIR TEMPERATURE  $T_a$  ACROSS SENSORS

Sensor	1	2	3	4	5	6	7	8	9
PCC	0.93	0.92	0.93	0.90	0.95	0.91	0.91	0.88	0.88
SRCC	0.94	0.93	0.89	0.85	0.94	0.91	0.88	0.85	0.87
Sensor	10	11	12	13	14	15	16	17	18
PCC	0.80	0.89	0.90	0.91	0.90	0.91	0.90	0.95	0.91
SRCC	0.80	0.88	0.88	0.93	0.90	0.92	0.87	0.93	0.94
Sensor	19	20	21	22	23	24	25	26	27
PCC	0.88	0.89	0.88	0.90	0.90	0.86	0.91	0.88	0.88
SRCC	0.85	0.86	0.85	0.87	0.88	0.88	0.91	0.85	0.85
Sensor	28	29	30	31	32	33	Average		
PCC	0.93	0.90	0.90	0.91	0.89	0.93	0.90		
SRCC	0.91	0.85	0.87	0.87	0.91	0.93	0.89		

WGAST's ability to reliably capture spatio-temporal variations in LST at fine spatial resolution.

Figure 8 displays scatter plots comparing WGAST's 10 m fused LST with ground-based air temperature ( $T_a$ ) from nine randomly selected sensors during the evaluation period. These plots demonstrate a strong correspondence between LST and  $T_a$ , which confirms that the fused LST product reliably captures the physical trends observed at ground level. The temporal evolution of LST and  $T_a$  shows a clear and synchronized pattern across all sensors. In almost every case, both LST and  $T_a$  exhibit the same monotonic behavior, with LST rising as  $T_a$  increases and following the same downward trend as  $T_a$  decreases. Even during periods of sharp thermal fluctuation, WGAST's LST closely tracks  $T_a$  by accurately detecting peaks and valleys across a variety spatial settings. Since the selected sensors span diverse land cover types, these results underscore the model's robustness and generalizability across diverse environments. Overall, the analysis validates the proposed method's ability to produce temporally coherent and physically realistic LST estimates in strong agreement with ground truth observations.

#### D. Qualitative Assessment

Figure 9 presents a qualitative comparison on 21 Oct 2024 between the 1 km Terra MODIS LST, the reference 30 m Landsat 8 LST, the 10 m LST generated by FuseTen and WGAST, and the corresponding high-resolution satellite image for visual context. We do not include other linear baselines, as their performance, evaluated through the visual metrics in Table V, was significantly inferior. Including them in this comparison would not provide meaningful insights.

In Figure 9.a, WGAST generates an LST distribution that aligns more closely with the reference Landsat 8 LST than FuseTen. WGAST preserves spatial coherence while enhancing fine details, particularly in capturing temperature gradients around urban hotspots (highlighted in red). Notably, the river's shape is sharply defined, with smooth yet well-preserved

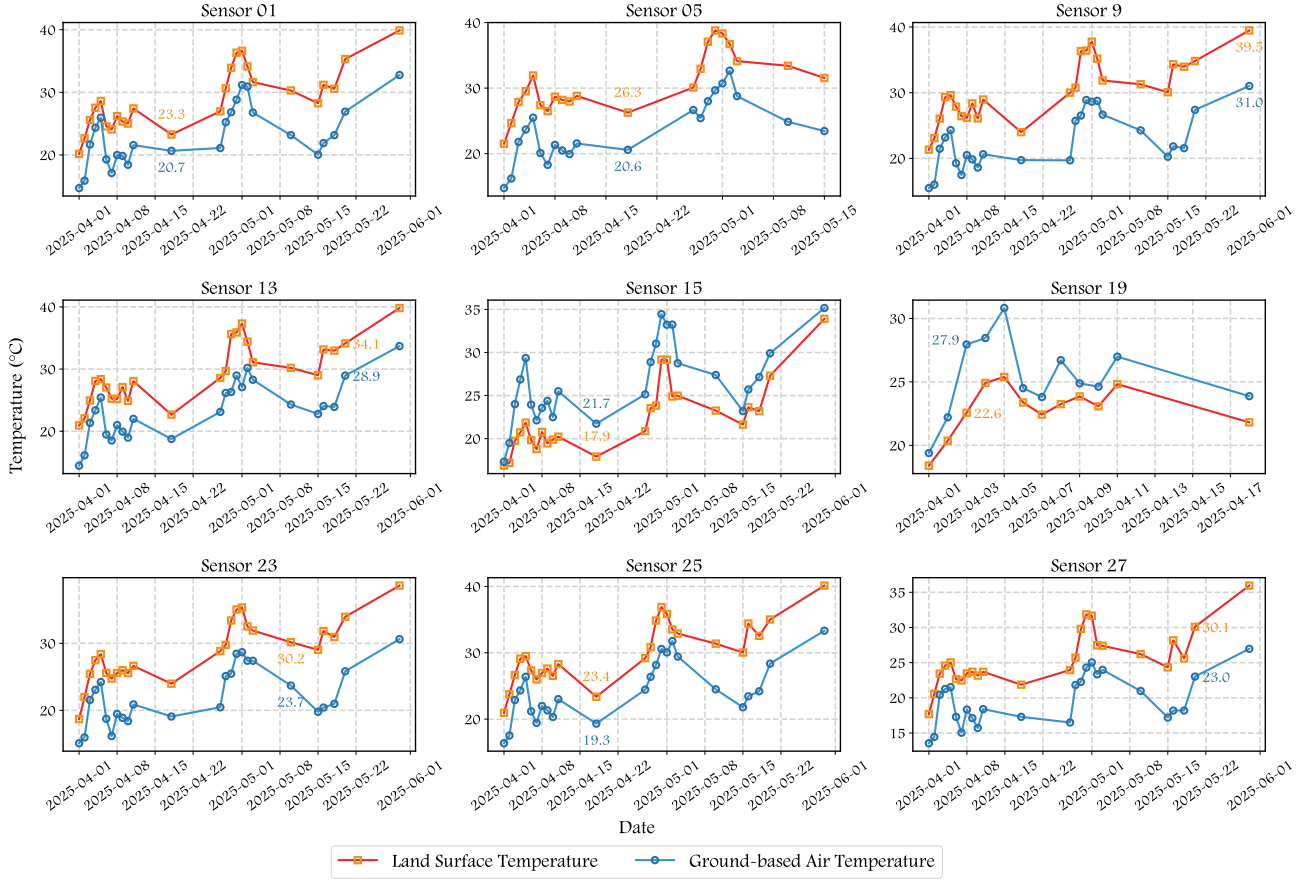


Fig. 8. Scatter plots comparing WGAST's 10 m LST with ground-based  $T_a$  from nine randomly selected sensors over the evaluation period. The plots illustrate the strong correlation and synchronized temporal dynamics between the generated LST and  $T_a$ .

thermal transition zones along its edges. In contrast, FuseTen tends to oversmooth these boundaries, resulting in the loss of critical spatial and thermal features, especially near the riverbanks. WGAST stands out by simultaneously maintaining fine structural edges and producing continuous, physically realistic thermal patterns, which are essential for accurately characterizing the UHI effect. Figure 9.b focuses on the Loire river as it passes through a semi-urban corridor of mixed built-up and vegetated areas. WGAST outperforms FuseTen by recovering the river's cool thermal signature and faithfully preserving its curved geometry along with the surrounding landscape features. The bridge crossing the river (highlighted in red) is sharply delineated in the WGAST LST, whereas it appears only faintly in the Landsat 8 LST and is practically invisible in FuseTen LST because of oversmoothing. FuseTen also underestimates the cooling effect of the water, yielding a flatter temperature field along the riverbanks. WGAST additionally excels in capturing the secondary river, Loiret (highlighted in blue), where the riverbanks are sharply delineated and correctly represented with cooler temperatures compared to the surrounding urban landscape. This thermal and structural contrast is hardly visible in the Landsat 8 LST reference. Figure 9.c focuses on a densely forested region in the Orléans Forest, the largest forest in France. WGAST delivers a remarkably detailed reconstruction of the thermal

structure of the forest by accurately capturing subtle intra-canopy temperature variations and preserving crisp spatial textures throughout the scene. The dense vegetation results in generally lower LST, and WGAST reflects this distribution with high fidelity. Notably, a vegetated zone exhibiting slightly elevated LST values compared to the rest of the forest (highlighted in red) is correctly reconstructed by WGAST, in alignment with the Landsat 8 LST reference. In contrast, FuseTen assigns a temperature to this area that is indistinguishable from surrounding forest regions thereby overlooking this zone. Figure 9.d depicts one of the most active industrial zones in Orléans Métropole, characterized by a dense configuration of industrial facilities, road networks, and fragmented green spaces. WGAST outperforms FuseTen by accurately capturing the thermal hotspots, particularly the regions highlighted in red. These areas align closely with the Landsat 8 LST reference. In contrast, FuseTen exhibits excessive smoothing, merging key thermal patterns, and diminishing the distinction between industrial and non-industrial zones. The area marked in blue corresponds to elevated LST values over a cluster of buildings, which WGAST successfully reconstructs by assigning significantly higher temperatures compared to the adjacent vegetated surfaces. However, FuseTen fails to emphasize this contrast, assigning nearly uniform temperatures that obscure the underlying land-use differences. Figure 9.e

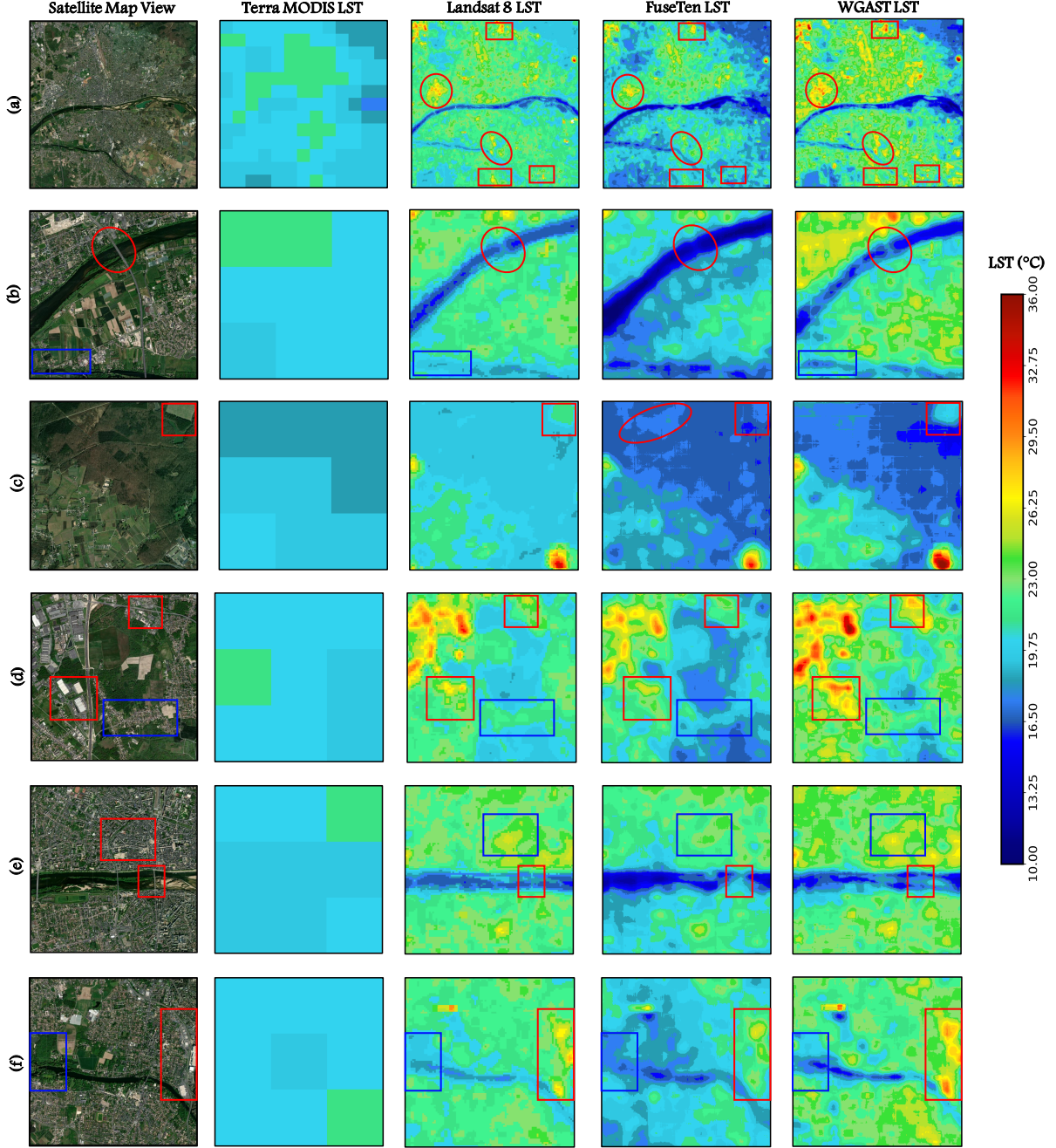


Fig. 9. Qualitative comparison of WGAST and FuseTen across six representative regions in Orléans Métropole on 21 Oct 2024: (a) the Orléans Métropole, (b) a semi-urban corridor along the Loire River, (c) the Orléans Forest, (d) a major industrial area, (e) the city center of Orléans, and (f) a mixed residential and vegetated neighborhood traversed by the Loire River. Each row displays the high-resolution satellite view alongside the Terra MODIS LST, the Landsat 8 LST reference, and the predictions from FuseTen and WGAST.

presents the city center of Orléans Métropole, a densely built urban environment traversed by the Loire river, along with numerous roads and bridge-like structures. WGAST demonstrates strong performance in preserving urban morphology and accurately capturing the elevated LST values typically associated with urban cores, as indicated in the region highlighted in blue. These temperature patterns are consistent with the Landsat 8 LST reference. In contrast, FuseTen not only underestimates the urban LST but also fails to reproduce the structural layout of the urban fabric. WGAST further restores

linear features such as roads and bridges with sharp detail, highlighted in red, while maintaining their thermal contrast relative to adjacent surfaces. The river itself remains clearly defined in the WGAST output, both spatially and thermally. However, FuseTen struggles to reconstruct this key feature. Figure 9.f depicts a heterogeneous urban landscape composed of small residential areas, streets, and open vegetated spaces, all intersected by the Loire River. WGAST accurately reflects the spatial diversity of the scene, clearly separating cool vegetated zones from warmer surfaces. In the red highlighted

area, WGAST successfully reconstructs a localized hotspot that is noticeably oversmoothed in FuseTen. Similarly, in the blue highlighted region, which corresponds to the river and its immediate surroundings, FuseTen assigns nearly uniform temperatures, failing to distinguish between water and adjacent land. In contrast, WGAST preserves the expected thermal gradient by accurately differentiating the cooler river from the warmer urban surfaces.

Overall, WGAST produces more physically coherent and realistic LST compared to FuseTen. It not only preserves fine spatial structures and thermal gradients, but also generates detailed daily 10 m LST that surpasses the 30 m Landsat reference, all from the much coarser 1 km Terra MODIS input.

Moreover, we observe that WGAST effectively addresses the issue of cloud gaps commonly found in Landsat 8 LST products, as shown in Figure 10. This is primarily due to its reliance solely on the Terra MODIS LST at the target time. Terra MODIS is less affected by persistent cloud cover compared to Landsat 8. As a result, WGAST can generate 10 m resolution LST that are not only temporally aligned with the Terra MODIS acquisition time but are also largely free from the cloud missing data that plagues Landsat 8 LST. Figure 10 highlights how WGAST successfully reconstructs physically plausible and high-resolution temperature fields in areas where Landsat 8 data are unavailable due to cloud contamination.

## V. CONCLUSION

In this work, we introduced WGAST, a Weakly-supervised Generative Network designed for daily 10 m LST estimation via STF of Terra MODIS, Landsat 8, and Sentinel-2. To the best of our knowledge, WGAST is the first fully DL-based model developed specifically for this task. The framework is built upon a cGAN, where the generator follows a four-stage pipeline: feature extraction, feature fusion, LST reconstruction, and noise suppression. A key contribution is the use of cosine similarity to guide the fusion by transferring relevance scores from Landsat 8 and Sentinel-2 spectral features to the Landsat 8 LST features. Training is guided by a weakly-supervised strategy based on physical averaging principles, where the generated 10 m LST is upsampled to 30 m and compared to Landsat 8 LST. It requires only Terra MODIS LST at the target time and a prior triplet  $T_1$  combining Terra MODIS, Landsat 8, and Sentinel-2, thus preserving the daily temporal resolution. WGAST outperforms existing methods both quantitatively and qualitatively. Compared to FuseTen, on average, it achieves a 17.18% reduction in RMSE, 4.10% improvement in SSIM, 11.00% increase in PSNR, and a 13.90% reduction in ERGAS, with even greater gains over traditional linear methods. It also preserves fine spatial details such as temperature gradients near rivers and bridges, variations around buildings, and structural patterns in industrial and agricultural areas. Additionally, by relying solely on Terra MODIS LST at the target time, WGAST overcomes cloud-induced gaps in Landsat 8 LST by producing complete, high-resolution, and physically consistent LST maps. Its reliability is further supported by the strong agreement between the generated 10 m LST maps and in situ measurements from 33 ground-based sensors across the ROI.

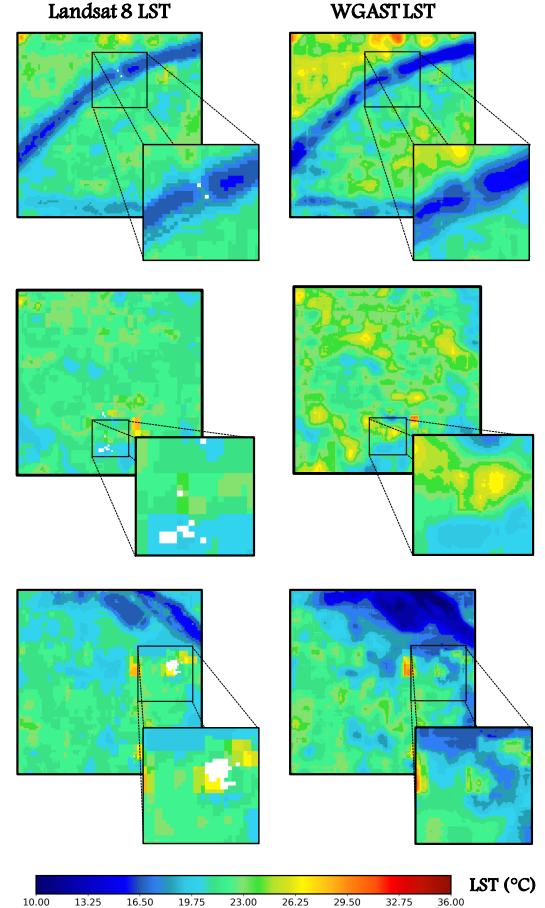


Fig. 10. WGAST reconstruction of cloud-covered regions in Landsat 8 LST on 21 Oct 2024. The comparison shows Landsat 8 LST (left column) and the corresponding WGAST predictions (right column) over three different regions. Zoomed-in areas highlight regions with missing data in Landsat due to clouds, which are reconstructed by WGAST.

Despite WGAST’s strong performance, its current training strategy is region-specific and may not generalize well to unseen areas with varying climatic zones. Future work will focus on developing an inference and transfer learning approach to enable automatic adaptation to unseen regions without full retraining. This would make the model more adaptable and suitable for large-scale and real-world deployment.

## REFERENCES

- [1] C. Folke, S. Polasky, J. Rockström, V. Galaz, F. Westley, M. Lamont, M. Scheffer, H. Österblom, S. R. Carpenter, F. S. Chapin *et al.*, “Our future in the anthropocene biosphere,” *Ambio*, vol. 50, pp. 834–869, 2021.
- [2] P. Singh, N. Kikon, and P. Verma, “Impact of land use change and urbanization on urban heat island in lucknow city, central india. a remote sensing based estimate,” *Sustainable cities and society*, vol. 32, pp. 100–114, 2017.
- [3] B. D. Sparrow, W. Edwards, S. E. Munroe, G. M. Wardle, G. R. Guerin, J.-F. Bastin, B. Morris, R. Christensen, S. Phinn, and A. J. Lowe, “Effective ecosystem monitoring requires a multi-scaled approach,” *Biological Reviews*, vol. 95, no. 6, pp. 1706–1719, 2020.
- [4] Y. Chu, M. Ye, and Y. Qian, “Fine-grained image recognition methods and their applications in remote sensing images: A review,” *IEEE Journal of Selected Topics in Applied Earth Observations and Remote Sensing*, 2024.

[5] F. Li, T. Yigitcanlar, M. Nepal, K. Nguyen, and F. Dur, "Machine learning and remote sensing integration for leveraging urban sustainability: A review and framework," *Sustainable Cities and Society*, vol. 96, p. 104653, 2023.

[6] V. V. Estrela, J. Aroma, R. Sroufer, K. Raimond, A. C. Intorne, A. Deshpande, A. A. Laghari, and L. P. Oliveira, "Remote sensing applications in disease mapping and public health analysis," in *Intelligent Healthcare Systems*. CRC Press, 2023, pp. 185–202.

[7] N. Kerle, "Disasters: Risk assessment, management, and post-disaster studies using remote sensing," in *Remote Sensing Handbook, Volume VI*. CRC Press, 2024, pp. 153–198.

[8] B. Sirmacek and R. Vinuesa, "Remote sensing and ai for building climate adaptation applications," *Results in Engineering*, vol. 15, p. 100524, 2022.

[9] S. Bouaziz, A. Hafiane, R. Canals, and R. Nedjai, "Deep learning for spatio-temporal fusion in land surface temperature estimation: A comprehensive survey, experimental analysis, and future trends," *arXiv preprint arXiv:2412.16631*, 2024.

[10] G. C. Hulley, D. Ghent, F. M. Götsche, P. C. Guillevic, D. J. Mildrexler, and C. Coll, "3 - land surface temperature," in *Taking the Temperature of the Earth*, G. C. Hulley and D. Ghent, Eds. Elsevier, 2019, pp. 57–127. [Online]. Available: <https://www.sciencedirect.com/science/article/pii/B9780128144589000034>

[11] D. K. Hall, J. C. Comiso, N. E. DiGirolamo, C. A. Shuman, J. R. Key, and L. S. Koenig, "A satellite-derived climate-quality data record of the clear-sky surface temperature of the greenland ice sheet," *Journal of Climate*, vol. 25, no. 14, pp. 4785–4798, 2012.

[12] S. Luyssaert, M. Jammel, P. C. Stoy, S. Estel, J. Pongratz, E. Ceschia, G. Churkina, A. Don, K. Erb, M. Ferlicoq *et al.*, "Land management and land-cover change have impacts of similar magnitude on surface temperature," *Nature Climate Change*, vol. 4, no. 5, pp. 389–393, 2014.

[13] M. Maimaitiyiming, A. Ghulam, T. Tiyip, F. Pla, P. Latorre-Carmona, Ü. Halik, M. Sawut, and M. Caetano, "Effects of green space spatial pattern on land surface temperature: Implications for sustainable urban planning and climate change adaptation," *ISPRS Journal of Photogrammetry and Remote Sensing*, vol. 89, pp. 59–66, 2014.

[14] M. King, *EOS Science Plan: The State of Science in the EOS Program*. National Aeronautics and Space Administration, 1999, available at: <https://books.google.fr/books?id=PS9RAAAAMA AJ>.

[15] R. Hollmann, C. J. Merchant, R. Saunders, C. Downy, M. Buchwitz, A. Cazenave, E. Chuvieco, P. Defourny, G. de Leeuw, R. Forsberg *et al.*, "The esa climate change initiative: Satellite data records for essential climate variables," *Bulletin of the American Meteorological Society*, vol. 94, no. 10, pp. 1541–1552, 2013.

[16] Z.-L. Li, B.-H. Tang, H. Wu, H. Ren, G. Yan, Z. Wan, I. F. Trigo, and J. A. Sobrino, "Satellite-derived land surface temperature: Current status and perspectives," *Remote sensing of environment*, vol. 131, pp. 14–37, 2013.

[17] J. Zhang and J. Li, "Chapter 11 - spacecraft," in *Spatial Cognitive Engine Technology*, J. Zhang and J. Li, Eds. Academic Press, 2023, pp. 129–162. [Online]. Available: <https://www.sciencedirect.com/science/article/pii/B9780323951074000044>

[18] P. Gibson, "Chapter 1 - a systematic view of remote sensing (second edition)," in *Advanced Remote Sensing*, S. Liang and J. Wang, Eds. Academic Press, 2020, pp. 1–57. [Online]. Available: <https://www.sciencedirect.com/science/article/pii/B9780128158265000015>

[19] X. Zhu, F. Cai, J. Tian, and T. K.-A. Williams, "Spatiotemporal fusion of multisource remote sensing data: Literature survey, taxonomy, principles, applications, and future directions," *Remote Sensing*, vol. 10, no. 4, p. 527, 2018.

[20] H. Song, Q. Liu, G. Wang, R. Hang, and B. Huang, "Spatiotemporal satellite image fusion using deep convolutional neural networks," *IEEE Journal of Selected Topics in Applied Earth Observations and Remote Sensing*, vol. 11, no. 3, pp. 821–829, 2018.

[21] R. Swain, A. Paul, and M. D. Behera, "Spatio-temporal fusion methods for spectral remote sensing: A comprehensive technical review and comparative analysis," *Tropical Ecology*, vol. 65, no. 3, pp. 356–375, 2024.

[22] F. Gao, J. Masek, M. Schwaller, and F. Hall, "On the blending of the landsat and modis surface reflectance: Predicting daily landsat surface reflectance," *IEEE Transactions on Geoscience and Remote sensing*, vol. 44, no. 8, pp. 2207–2218, 2006.

[23] X. Zhu, J. Chen, F. Gao, X. Chen, and J. G. Masek, "An enhanced spatial and temporal adaptive reflectance fusion model for complex heterogeneous regions," *Remote Sensing of Environment*, vol. 114, no. 11, pp. 2610–2623, 2010.

[24] H. Liu and Q. Weng, "Enhancing temporal resolution of satellite imagery for public health studies: A case study of west nile virus outbreak in los angeles in 2007," *Remote Sensing of environment*, vol. 117, pp. 57–71, 2012.

[25] Y. Ma, S. Liu, L. Song, Z. Xu, Y. Liu, T. Xu, and Z. Zhu, "Estimation of daily evapotranspiration and irrigation water efficiency at a landsat-like scale for an arid irrigation area using multi-source remote sensing data," *Remote Sensing of Environment*, vol. 216, pp. 715–734, 2018.

[26] B. Mohamadi, S. Chen, T. Balz, K. Gulshad, and S. C. McClure, "Normalized method for land surface temperature monitoring on coastal reclaimed areas," *Sensors*, vol. 19, no. 22, p. 4836, 2019.

[27] Z. Yin, P. Wu, G. M. Foody, Y. Wu, Z. Liu, Y. Du, and F. Ling, "Spatiotemporal fusion of land surface temperature based on a convolutional neural network," *IEEE Transactions on Geoscience and Remote Sensing*, vol. 59, no. 2, pp. 1808–1822, 2020.

[28] Y. Chen, Y. Yang, X. Pan, X. Meng, and J. Hu, "Spatiotemporal fusion network for land surface temperature based on a conditional variational autoencoder," *IEEE Transactions on Geoscience and Remote Sensing*, vol. 60, pp. 1–13, 2022.

[29] P. Hu, X. Pan, Y. Yang, Y. Dai, and Y. Chen, "A two-stage hierarchical spatiotemporal fusion network for land surface temperature with transformer," *IEEE Transactions on Geoscience and Remote Sensing*, 2025.

[30] I. Goodfellow, J. Pouget-Abadie, M. Mirza, B. Xu, D. Warde-Farley, S. Ozair, A. Courville, and Y. Bengio, "Generative adversarial nets," *Advances in neural information processing systems*, vol. 27, 2014.

[31] H. Zhang, Y. Song, C. Han, and L. Zhang, "Remote sensing image spatiotemporal fusion using a generative adversarial network," *IEEE Transactions on Geoscience and Remote Sensing*, vol. 59, no. 5, pp. 4273–4286, 2020.

[32] Z. Tan, M. Gao, X. Li, and L. Jiang, "A flexible reference-insensitive spatiotemporal fusion model for remote sensing images using conditional generative adversarial network," *IEEE Transactions on Geoscience and Remote Sensing*, vol. 60, pp. 1–13, 2021.

[33] J. Chen, L. Wang, R. Feng, P. Liu, W. Han, and X. Chen, "Cyclegan-stf: Spatiotemporal fusion via cyclegan-based image generation," *IEEE Transactions on Geoscience and Remote Sensing*, vol. 59, no. 7, pp. 5851–5865, 2020.

[34] B. Song, P. Liu, J. Li, L. Wang, L. Zhang, G. He, L. Chen, and J. Liu, "Mlff-gan: A multilevel feature fusion with gan for spatiotemporal remote sensing images," *IEEE Transactions on Geoscience and Remote Sensing*, vol. 60, pp. 1–16, 2022.

[35] D. P. Roy, M. A. Wulder, T. R. Loveland, C. E. Woodcock, R. G. Allen, M. C. Anderson, D. Helder, J. R. Irons, D. M. Johnson, R. Kennedy *et al.*, "Landsat-8: Science and product vision for terrestrial global change research," *Remote sensing of Environment*, vol. 145, pp. 154–172, 2014.

[36] H. Shi, G. Xian, R. Auch, K. Gallo, and Q. Zhou, "Urban heat island and its regional impacts using remotely sensed thermal data—a review of recent developments and methodology," *Land*, vol. 10, no. 8, p. 867, 2021.

[37] D. Zhou, J. Xiao, S. Bonafoni, C. Berger, K. Deilami, Y. Zhou, S. Frolking, R. Yao, Z. Qiao, and J. A. Sobrino, "Satellite remote sensing of surface urban heat islands: Progress, challenges, and perspectives," *Remote Sensing*, vol. 11, no. 1, p. 48, 2018.

[38] M. Mhawej and Y. Abunnasr, "Daily ten-st-gee: An open access and fully automated 10-m 1st downscaling system," *Computers & Geosciences*, vol. 168, p. 105220, 2022.

[39] D. Xiang, Y. Sun, H. Zhu, J. Wang, S. Huang, S. Zhang, F. Zhang, and H. Zhang, "Comparative analysis of prediction models for trawling grounds of the argentine shortfin squid *illex argentinus* in the southwest atlantic high seas based on vessel position and fishing log data," *Biology*, vol. 14, no. 1, p. 35, 2025.

[40] S. Bouaziz, A. Hafiane, R. Canals, and R. Nedjai, "Fuseten: A generative model for daily 10 m land surface temperature estimation from spatiotemporal satellite observations," *arXiv preprint arXiv:2507.23154*, 2025.

[41] S. Guha, H. Govil, A. K. Taloor, N. Gill, and A. Dey, "Land surface temperature and spectral indices: A seasonal study of raipur city," *Geodesy and Geodynamics*, vol. 13, no. 1, pp. 72–82, 2022.

[42] A. J. Abdalkadhum, M. M. Salih, and O. Z. Jasim, "The correlation among land cover spectral indices and surface temperature using remote sensing techniques," in *IOP Conference Series: Materials Science and Engineering*, vol. 1090, no. 1. IOP Publishing, 2021, p. 012024.

[43] P. Sharma, M. Kumar, H. K. Sharma, and S. M. Biju, "Generative adversarial networks (gans): Introduction, taxonomy, variants, limitations, and applications," *Multimedia Tools and Applications*, pp. 1–48, 2024.

- [44] Y. Hong, U. Hwang, J. Yoo, and S. Yoon, "How generative adversarial networks and their variants work: An overview," *ACM Computing Surveys (CSUR)*, vol. 52, no. 1, pp. 1–43, 2019.
- [45] Y.-P. Hsieh, C. Liu, and V. Cevher, "Finding mixed nash equilibria of generative adversarial networks," in *International Conference on Machine Learning*. PMLR, 2019, pp. 2810–2819.
- [46] M. Mirza and S. Osindero, "Conditional generative adversarial nets," *arXiv preprint arXiv:1411.1784*, 2014.
- [47] B. Lim, S. Son, H. Kim, S. Nah, and K. Mu Lee, "Enhanced deep residual networks for single image super-resolution," in *Proceedings of the IEEE conference on computer vision and pattern recognition workshops*, 2017, pp. 136–144.
- [48] X. Huang and S. Belongie, "Arbitrary style transfer in real-time with adaptive instance normalization," in *Proceedings of the IEEE international conference on computer vision*, 2017, pp. 1501–1510.
- [49] L. Gao, W. Zhan, F. Huang, J. Quan, X. Lu, F. Wang, W. Ju, and J. Zhou, "Localization or globalization? determination of the optimal regression window for disaggregation of land surface temperature," *IEEE Transactions on Geoscience and Remote Sensing*, vol. 55, no. 1, pp. 477–490, 2016.
- [50] X. Mao, Q. Li, H. Xie, R. Y. Lau, Z. Wang, and S. Paul Smolley, "Least squares generative adversarial networks," in *Proceedings of the IEEE international conference on computer vision*, 2017, pp. 2794–2802.
- [51] N. Gorelick, M. Hancher, M. Dixon, S. Ilyushchenko, D. Thau, and R. Moore, "Google earth engine: Planetary-scale geospatial analysis for everyone," *Remote sensing of Environment*, vol. 202, pp. 18–27, 2017.
- [52] S.-B. Duan, Z.-L. Li, H. Li, F.-M. Götsche, H. Wu, W. Zhao, P. Leng, X. Zhang, and C. Coll, "Validation of collection 6 modis land surface temperature product using in situ measurements," *Remote sensing of environment*, vol. 225, pp. 16–29, 2019.
- [53] J. C. Jimenez-Munoz, J. A. Sobrino, D. Skoković, C. Mattar, and J. Cristobal, "Land surface temperature retrieval methods from landsat-8 thermal infrared sensor data," *IEEE Geoscience and remote sensing letters*, vol. 11, no. 10, pp. 1840–1843, 2014.
- [54] I. Cohen, Y. Huang, J. Chen, J. Benesty, J. Benesty, J. Chen, Y. Huang, and I. Cohen, "Pearson correlation coefficient," *Noise reduction in speech processing*, pp. 1–4, 2009.
- [55] J. H. Zar, "Spearman rank correlation: overview," *Wiley StatsRef: Statistics Reference Online*, 2014.



**Sofiane Bouaziz** is PhD Student at INSA Centre Val de Loire (INSA CVL) and the PRISME Laboratory. He received his Master's and Engineering degrees in Computer Science and Artificial Intelligence from École Nationale Supérieure d'Informatique, Algiers, Algeria in 2023. His current research focuses on using Artificial Intelligence and Computer Vision to tackle challenges in remote sensing.



**Adel Hafiane** received the M.S. degree in embedded systems and information processing, and the Ph.D. degree from the University of Paris-Saclay, in 2002 and 2005, respectively. After that, he embarked on teaching and research, spending a year at Paris-Saclay and subsequently another year at INSA Centre Val de Loire (INSA CVL). He was postdoctoral fellow at the computer science department, University of Missouri, from 2007 to 2008. Since September 2008, as an assistant professor, then as an associate professor. He is a head of the Image and Vision group at PRISME Laboratory of University of Orléans and INSA CVL. He was an invited researcher at the University of Missouri on multiple periods, from 2009 to 2013. His research interests include theory and methods of machine learning and computer vision for different applications. He coordinated several research projects and co-authored more than 90 papers and 3 patents. He has also served as an associate editor for several special issues in remote sensing.



**Raphaël Canals** received the Dipl.Ing. degree in electrical engineering and the Ph.D. degree in electronics from the University of ClermontFerrand, France, in 1989 and 1993, respectively. In 1993, he was Postdoctoral Fellow at the Computer Science Department, CNRC, Ottawa, ON, Canada. In 1994, he joined the Polytechnic School, University of Orléans, France, as a Teacher. He is currently a Researcher with Laboratoire PRISME, University of Orléans-INSA CVL. He is also an Associate Professor with the University of Orléans. In 2015, he was introduced at the AgreeTech Valley Cluster dedicated to digital technologies for plant industry. His current interests are in biomedical imaging, innovation for agriculture, the IoT, and AI.



**Rachid Nedjai** is a professor in limnology and geomatics at the University of Orléans, where he also leads the Master's program in Geographic Information Systems (GAED). He obtained his Ph.D. in geochemistry of lacustrine waters and paleoenvironmental reconstruction from the University of Grenoble 1. His research focuses on environmental data simulation, hydrogeology, and geomatics applications for water resource management. He has contributed to numerous international projects, including the redesign of Algeria's judicial map and a spatial data infrastructure for water management in Africa. He has supervised multiple theses on hydrology, water resource management, and environmental risk assessment, with many of his students successfully entering the professional world. His expertise in geomatics and water resource management has made him a key contributor to advancing sustainable practices in the field.